

Observation of the antimatter helium-4 nucleus *(submitted to Nature, under media embargo)*

High-energy nuclear collisions create an energy density similar to that of the universe microseconds after the Big Bang¹, and in both cases, matter and antimatter are formed with comparable abundance. However, the relatively short-lived expansion in nuclear collisions allows antimatter to decouple quickly from matter, and avoid annihilation. Thus, a high-energy accelerator of heavy nuclei is an efficient means of producing and studying antimatter. The antimatter helium-4 nucleus (${}^4\overline{\text{He}}$), also known as the anti- α ($\overline{\alpha}$), consists of two antiprotons and two antineutrons (baryon number $B = -4$). It has not been observed previously, although the α particle was identified a century ago by Rutherford and is present in cosmic radiation at the 10% level². Antimatter nuclei with $B < -1$ have been observed only as rare products of interactions at particle accelerators, where the rate of antinucleus production in high-energy collisions decreases by about 1000 with each additional antinucleon³⁻⁵. We present the observation of the antimatter helium-4 nucleus, the heaviest observed antinucleus. In total 18 ${}^4\overline{\text{He}}$ counts were detected at the STAR experiment at RHIC⁶ in 10^9 recorded gold on gold (Au+Au) collisions at center-of-mass energies of 200 GeV and 62 GeV per nucleon-nucleon pair. The yield is consistent with expectations from thermodynamic⁷ and coalescent nucleosynthesis⁸ models, which has implications beyond nuclear physics.

In 1928, Dirac⁹ predicted the existence of negative energy states of electrons based on the application of symmetry principles to quantum mechanics, but only recognized these states to be antimatter after Anderson's¹⁰ discovery of the positron (the antielectron) in cosmic radiation four

years later. The predicted antiprotons¹¹ and antineutrons¹² were observed in 1955, followed by antideuterons (\bar{d}), antitritons (${}^3\bar{H}$), and antihelium-3 (${}^3\bar{He}$) during the following two decades¹³⁻¹⁶. Recent accelerator and detector advances led to the first production of antihydrogen¹⁷ atoms in 1995 and the discovery of strange antimatter, the antihypertriton (${}^3_{\Lambda}\bar{H}$), in 2010 at the Relativistic Heavy Ion Collider (RHIC) at Brookhaven National Laboratory (BNL)¹⁸.

Collisions of relativistic heavy nuclei create suitable conditions for producing antinuclei, because large amounts of energy are deposited into a more extended volume¹⁹ than that achieved in elementary particle collisions. These nuclear interactions briefly ($\sim 10^{-23}$ seconds) produce hot and dense matter containing roughly equal numbers of quarks and antiquarks²⁰, often interpreted as quark gluon plasma (QGP)²¹. In contrast to the Big Bang, nuclear collisions produce negligible gravitational attraction and allow the plasma to expand rapidly. The hot and dense matter cools down and transitions into a hadron gas, producing nucleons and their antiparticles. The production of light antinuclei can be modeled successfully by macroscopic thermodynamics⁷, which assumes energy equipartition, or by a microscopic coalescence process^{8,22}, which assumes uncorrelated probabilities for antinucleons close in position and momentum to become bound. The high temperature and high antibaryon density of relativistic heavy ion collisions provide a favorable environment for both production mechanisms.

The central detector used in our measurements of antimatter, the Time Projection Chamber (TPC)²³ of the STAR experiment (Solenoidal Tracker At RHIC), is situated in a solenoidal magnetic field and is used for three-dimensional imaging of the ionization trail left along the path of

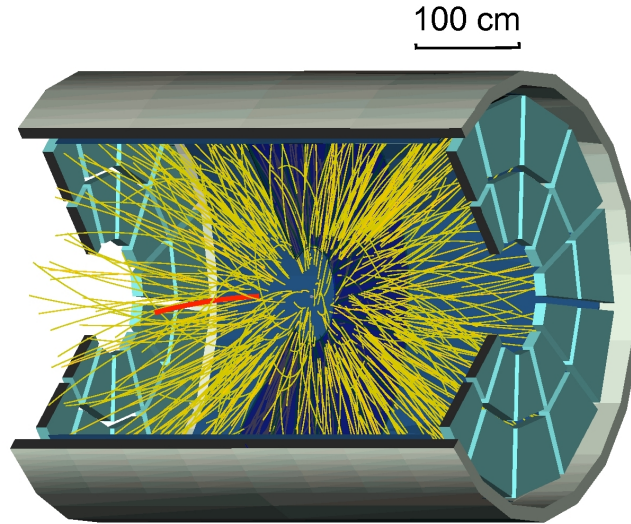


Figure 1: A three-dimensional rendering of the STAR TPC surrounded by the TOF barrel shown as the outermost cylinder. Tracks from an event which contains a ${}^4\overline{\text{He}}$ are shown, with the ${}^4\overline{\text{He}}$ track highlighted in bold red.

charged particles (Fig. 1). In addition to the momentum provided by the track curvature in the magnetic field, the detection of ${}^4\overline{\text{He}}$ particles relies on two key measurements: the mean energy loss per unit track length $\langle dE/dx \rangle$ in the TPC gas, which helps distinguish particles with different masses or charges, and the time of flight of particles arriving at the time of flight barrel (TOF)²⁴ surrounding the TPC. In general, time of flight provides particle identification in a higher momentum range than $\langle dE/dx \rangle$. The $\langle dE/dx \rangle$ resolution is 7.5% and the timing resolution for TOF is 95 picoseconds.

The trigger system at STAR selects collisions of interest for analysis. The minimum-bias

(MB) trigger selects all particle-producing collisions, regardless of the extent of overlap of the incident nuclei. A central trigger (CENT) preferentially selects head-on collisions, rejecting about 90% of the events acquired using the MB trigger. The sample of 10^9 Au+Au collisions used in this search is selected based on MB, CENT, and on various specialized triggers. Preferential selection of events containing tracks with charge $Ze = \pm 2e$ (where e is the electron charge) was implemented using a High-Level Trigger (HLT) for data acquired in 2010. The HLT used computational resources at STAR to perform a real-time fast track reconstruction to tag events that had at least one track with a $\langle dE/dx \rangle$ value that is larger than a threshold set to three standard deviations below the theoretically expected value²⁵ for ${}^3\overline{\text{He}}$ at the same momentum. The HLT successfully identified 70% of the events where a ${}^4\overline{\text{He}}$ track was present while selecting only 0.4% of the events for express analyses.

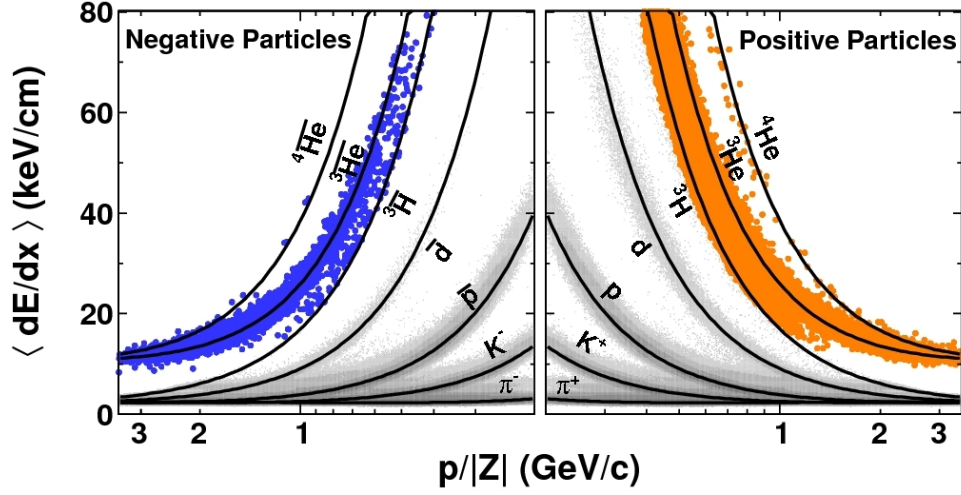


Figure 2: $\langle dE/dx \rangle$ versus $p/|Z|$ for negatively charged particles (left) and positively charged particles (right). The black curves show the expected values for each species. The lower edges of the colored bands correspond to the HLT's online calculation of 3σ below the $\langle dE/dx \rangle$ band center²⁵ for ${}^3\text{He}$.

Figure 2 shows $\langle dE/dx \rangle$ versus the magnitude of magnetic rigidity, $p/|Z|$, where p is momentum. A distinct band of positive particles centered around the expected value²⁵ for ${}^4\text{He}$ particles indicates that the detector is well-calibrated. On the left side of Fig. 2, where $p/|Z|$ is less than 1.4 GeV/c, four negative particles are particularly well separated from the ${}^3\text{He}$ band and are located within the expected band for ${}^4\text{He}$. Above 1.75 GeV/c, $\langle dE/dx \rangle$ values of ${}^3\text{He}$ and ${}^4\text{He}$ merge and the TOF system is needed to separate these two species.

The top two panels of Fig. 3 shows the $\langle dE/dx \rangle$ (in units of multiples of $\sigma_{dE/dx}$, $n_{\sigma_{dE/dx}}$) versus calculated mass $m = (p/c)\sqrt{(t^2c^2/L^2 - 1)}$, where $\sigma_{dE/dx}$ is the rms width of the $\langle dE/dx \rangle$

distribution for ${}^4\text{He}$ or ${}^4\overline{\text{He}}$, t and L are the time of flight and path length, respectively, and c is the speed of light. The first (second) panel shows negatively (positively) charged particles. In both panels, majority species are ${}^3\text{He}$ and ${}^3\overline{\text{He}}$. In the second panel, the ${}^4\text{He}$ particles cluster around $n_{\sigma_{dE/dx}} = 0$ and mass = $3.73 \text{ GeV}/c^2$, the appropriate mass for ${}^4\text{He}$. A similar but smaller cluster of particles can be found in the first panel for ${}^4\overline{\text{He}}$. The bottom panel shows the projection onto the mass axis of the top two panels for particles with $n_{\sigma_{dE/dx}}$ of -2 to 3. There is clear separation between ${}^3\overline{\text{He}}$ and ${}^4\overline{\text{He}}$ mass peaks. Eighteen counts for ${}^4\overline{\text{He}}$ are observed. Of those, sixteen are from collisions recorded in 2010. Two counts²⁶ identified by $\langle dE/dx \rangle$ alone from data recorded in 2007 are not included in this figure, because the STAR TOF was not installed at that time.

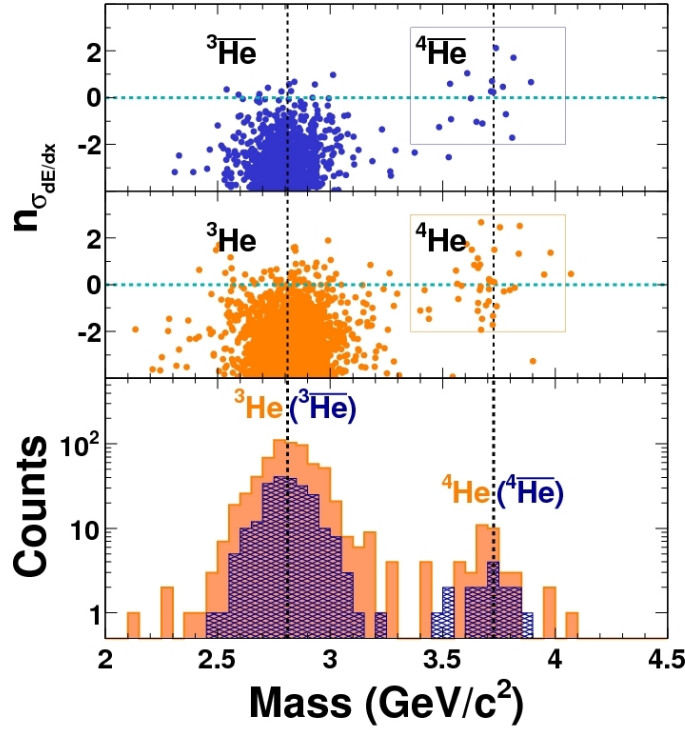


Figure 3: The top two panels show the $\langle dE/dx \rangle$ in units of multiples of $\sigma_{dE/dx}$, $n_{\sigma_{dE/dx}}$, of negatively charged particles (first panel) and positively charged particles (second panel) as a function of mass measured by the TOF system. The masses of ${}^3\text{He}$ (${}^3\overline{\text{He}}$) and ${}^4\text{He}$ (${}^4\overline{\text{He}}$) are indicated by the vertical lines at $2.81 \text{ GeV}/c^2$ and $3.73 \text{ GeV}/c^2$, respectively. The horizontal line marks the position of zero deviation from the expected value of $\langle dE/dx \rangle$ ($n_{\sigma_{dE/dx}} = 0$) for ${}^4\text{He}$ (${}^4\overline{\text{He}}$). The rectangular boxes highlight areas for ${}^4\text{He}$ (${}^4\overline{\text{He}}$) selections : $-2 < n_{\sigma_{dE/dx}} < 3$ and $3.35 \text{ GeV}/c^2 < \text{mass} < 4.04 \text{ GeV}/c^2$ (corresponding to a $\pm 3\sigma$ window in mass). The bottom panel shows a projection of entries in the upper two panels onto the mass axis for particles in the window of $-2 < \sigma_{dE/dx} < 3$. The combined measurements of energy loss and the time of flight allow a clean identification to be made in a sample of 0.5×10^{12} tracks from 10^9 Au+Au collisions.

To evaluate the background in ${}^4\overline{\text{He}}$ due to ${}^3\overline{\text{He}}$ contamination, we simulate the ${}^3\overline{\text{He}}$ mass distribution with momenta and path lengths, as well as the expected time of flight from ${}^3\overline{\text{He}}$ particles with timing resolution derived from the same data sample. The contamination from misidentifying ${}^3\overline{\text{He}}$ as ${}^4\overline{\text{He}}$ is estimated by integrating over the region of the ${}^4\overline{\text{He}}$ selection. We estimate that the background contributes 1.4 (0.05) counts of the 15 (1) total counts from Au+Au collisions at 200 (62) GeV recorded in 2010.

The observed counts are used to calculate the antimatter yield with appropriate normalization (the differential invariant yield) in order to compare to the theoretical expectation. Detector acceptance, efficiency, and antimatter annihilation with the detector material are taken into account when computing yields. Various uncertainties related to tracking in the TPC, matching in the TOF, and triggering in the HLT are cancelled when the yield ratios of ${}^4\text{He}/{}^3\text{He}$ and ${}^4\overline{\text{He}}/{}^3\overline{\text{He}}$ are calculated. The ratios are ${}^4\text{He}/{}^3\text{He} = (3.0 \pm 1.3(\text{stat})_{-0.3}^{+0.5}(\text{sys})) \times 10^{-3}$ and ${}^4\overline{\text{He}}/{}^3\overline{\text{He}} = (3.2 \pm 2.3(\text{stat})_{-0.2}^{+0.7}(\text{sys})) \times 10^{-3}$ for central Au+Au collisions at 200 GeV. The ratios were obtained in a window $40^\circ < \theta < 140^\circ$, where polar angle, θ , is the angle between the particle's momentum vector and the beam axis (these θ limits correspond to limits of -1 to 1 in a related quantity, pseudorapidity), and in a p_T per baryon window centered at $p_T/|B| = 0.875 \text{ GeV}/c$ with a width of $0.25 \text{ GeV}/c$, where p_T is the projection of the momentum vector on the plane that is transverse to the beam axis. Ratios calculated by a Blastwave model²⁷ for the $p_T/|B|$ window mentioned above and for the whole range of $p_T/|B|$ differ by only 1%. The differential yields ($d^2N/(p_T dp_T dy)$) for ${}^4\text{He}$ (${}^4\overline{\text{He}}$) are obtained by multiplying the ratio of ${}^4\text{He}/{}^3\text{He}$ (${}^4\overline{\text{He}}/{}^3\overline{\text{He}}$) with the ${}^3\text{He}$ (${}^3\overline{\text{He}}$) yields²⁸. The systematic uncertainties consist of background (-6% for both ratios),

feed-down from (anti-)hypertritons (18% for both ${}^3\text{He}$ and ${}^3\overline{\text{He}}$), knock-outs from beam-material interactions (-5% for the ratio ${}^4\text{He}/{}^3\text{He}$ only) and absorption (4% for the ratio ${}^4\overline{\text{He}}/{}^3\overline{\text{He}}$ only). Figure 4 shows the exponential³ invariant yields versus baryon number in 200 GeV central Au+Au collisions. Empirically, the production rate reduces by a factor of $1.6_{-0.6}^{+1.0} \times 10^3$ ($1.1_{-0.2}^{+0.3} \times 10^3$) for each additional antinucleon (nucleon) added to the antinucleus (nucleus). This general trend is expected from coalescent nucleosynthesis models⁸, originally developed to describe production of antideuterons²², and as well as from thermodynamic models⁷.

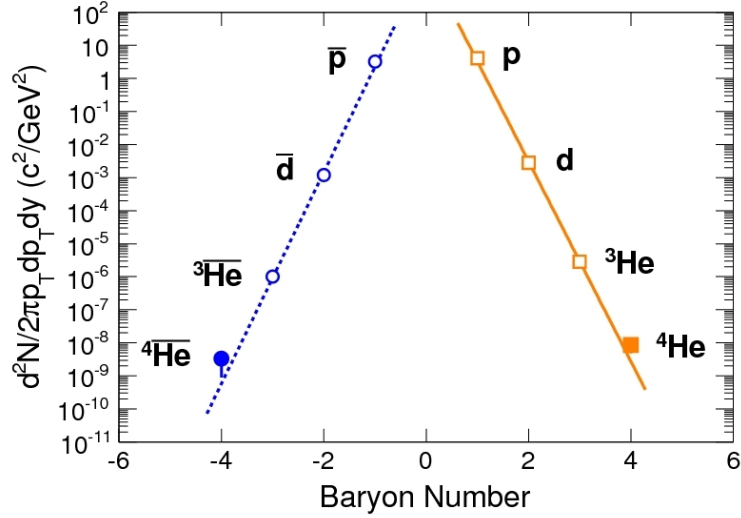


Figure 4: Differential invariant yields as a function of baryon number B , evaluated at $p_T/|B| = 0.875$ GeV/ c , in central 200 GeV Au+Au collisions. Yields for (anti)tritons (${}^3\text{H}$ and ${}^3\overline{\text{H}}$) lie close to the positions for ${}^3\text{He}$ and ${}^3\overline{\text{He}}$, but are not included here because of poorer identification of (anti)tritons. The lines represent fits with the exponential formula $\propto e^{-r|B|}$ for positive and negative particles separately, where r is the production reduction factor. Analysis details of yields other than ${}^4\text{He}$ (${}^4\overline{\text{He}}$) have been presented elsewhere^{4,28}. Errors are statistical only. Systematic errors are smaller than the symbol size, and are not plotted.

In a microscopic picture, a light nucleus emerging from a relativistic heavy-ion collision is produced during the last stage of the collision process. The quantum wave functions of the constituent nucleons, if close enough in momentum and coordinate space, will overlap to produce the nucleus. The production rate for a nucleus with baryon number B is proportional to the nucleon density in momentum and coordinate space, raised to the power of $|B|$, and therefore exhibits exponential behaviour as a function of B . Alternatively, in a thermodynamic model, a nucleus is regarded as an object with energy $E \sim |B|m_N$, where m_N is the nucleon mass, and the production rate is determined by the Boltzmann factor $\exp(-E/T)$, where T is the temperature^{3,7}. This model also produces an exponential yield. A more rigorous calculation⁵ can provide a good fit to the available particle yields and predicts the ratios integrated over p_T to be ${}^4\text{He}/{}^3\text{He} = 3.1 \times 10^{-3}$ and ${}^4\overline{\text{He}}/{}^3\overline{\text{He}} = 2.4 \times 10^{-3}$, consistent with our measurements. The considerations outlined above offer a good estimate for the production rate of even heavier antinuclei. For example, the yield of the stable antimatter nucleus next in line ($B = -6$) is predicted to be down by a factor of 2.6×10^6 compared to ${}^4\overline{\text{He}}$ and is beyond the reach of current accelerator technology.

A potentially more copious production mechanism for heavier antimatter is by the direct excitation of complex nuclear structures from the vacuum²⁹. A deviation from the usual rate reduction with increasing mass would be an indication of a radically new production mechanism⁷. On the other hand, going beyond nuclear physics, the sensitivity of current and planned space-based charged particle detectors is below what would be needed to observe antihelium produced by nuclear interactions in the cosmos, and consequently, any observation of antihelium or even heavier antinuclei in space would indicate the existence of a large amount of antimatter elsewhere

in the universe. In particular, finding ${}^4\overline{\text{He}}$ in the cosmos is one of the major motivations for space detectors such as the Alpha Magnetic Spectrometer³⁰. We have shown that ${}^4\overline{\text{He}}$ exists, and have measured its rate of production in nuclear interactions, providing a point of reference for possible future observations in cosmic radiation. Barring one of those dramatic discoveries mentioned above or new breakthrough in the accelerator technology, it is likely that the ${}^4\overline{\text{He}}$ will remain the heaviest stable antimatter nucleus observed for the foreseeable future.

1. Lemaître, G., A homogeneous universe of constant mass and increasing radius accounting for the radial velocity of extragalactic nebulae (in French). *Annales de la société Scientifique de Bruxelles* **47**, 49 (1927).
2. Wiebel-Sooth, B., Biermann, P. and Meyer, H., Cosmic rays, VII. Individual element spectra: prediction and data. *Astron. Astrophysics* **330**, 389 (1998), and references therein.
3. Armstrong, T. A. *et al.*, E864 Collaboration, Mass dependence of light-nucleus production in ultrarelativistic heavy-ion collisions. *Phys. Rev. Lett.* **83**, 5431(1999).
4. Liu, H., Production of meson, baryon and light nuclei (A=2,3): investigating freeze-out dynamics and roles of energetic quarks and gluons in Au+Au collisions at RHIC. Ph.D. thesis, University of Science and Technology of China, (2007).
5. Andronic, A., Braun-Munzinger, P., Stachel, J. and Stöcker, H., Production of light nuclei, hypernuclei and their antiparticles in relativistic nuclear collisions. *Phys. Lett. B* **697**, 203 (2011).

6. Harrison, M., Ludlam, T. and Ozaki, S., The relativistic heavy ion collider project: RHIC and its detectors. *Nucl. Instr. and Meth. in Phys. Res. A* **499** (2003).
7. Braun-Munzinger, P. and Stachel, J., The quest for the quark-gluon plasma. *Nature* **448**, 302 (2007).
8. Sato, H. and Yazaki, K., On the coalescence model for high energy nuclear reactions. *Phys. Lett. B* **98**, 153 (1981).
9. Dirac, P.A.M., The Quantum Theory of the Electron. *Proc. Roy. Soc. Lond. A* **117**, 610 (1928).
10. Anderson, C.D., The positive electron. *Phys. Rev.* **43**, 491 (1933).
11. Chamberlain, O., Segrè, E., Wiegand, C., and Ypsilantis, T., Observation of antiprotons. *Phys. Rev.* **100**, 947 (1955).
12. Cork, B., Lambertson, G. R., Piccioni, O., Wenzel, W. A., Antineutrons produced from antiprotons in charge-exchange collisions. *Phys. Rev.* **104**, 1193 (1956).
13. Massam, T., Muller, T., Righini, B., Schneegans, M., Zichichi, A., Experimental observation of antideuteron production. *Nuovo Cimento* **39**, 10 (1965).
14. Dorfan, D.E., Eades, J., Lederman, L.M., Lee, W., Ting, C.C., Observation of antideuterons. *Phys. Rev. Lett.* **14**, 1003 (1965).
15. Vishnevsky, N. K. *et al.*, Observation of antitritium (in Russian). *Yad. Fiz.* **20**, 694 (1974).
16. Antipov, Y. M. *et al.*, Observation of antihelium3 (in Russian). *Yad. Fiz.* **12**, 311 (1970).

17. Baur, G. *et al.*, Production of antihydrogen. *Phys. Lett. B* **368**, 251 (1996).
18. Abelev, B. I. *et al.*, STAR Collaboration, Observation of an antimatter hypernucleus. *Science* **328**, 58 (2010), and references therein.
19. Lee, T.D., Abnormal nuclear states and vacuum excitation. *Rev. Mod. Phys.* **47**, 267 (1975).
20. BRAHMS, PHENIX, PHOBOS, and STAR Collaboration, RHIC white papers. *Nucl. Phys. A* **757**, Issues 1-2 (2005).
21. Heinz, U., Subramanian, P.R., Stöcker, H. and Greiner, W., Formation of antimatter clusters in the hadronization phase transition. *J. Phys. G* **12**, 1237 (1986).
22. Butler, S.T. and Pearson, C.A., Deuterons from high-energy proton bombardment of matter. *Phys. Rev. Lett.* **7**, 69 (1961).
23. Anderson, M. *et al.*, The STAR time projection chamber: a unique tool for studying high multiplicity events at RHIC. *Nucl. Instr. and Meth. in Phys. Res. A* **499**, 659 (2003).
24. Bonner, B. *et al.*, A single Time-of-Flight tray based on multigap resistive plate chambers for the STAR experiment at RHIC. *Nucl. Instr. and Meth. in Phys. Res. A* **508**, 181 (2003).
25. Bichsel, H., A method to improve tracking and particle identification in TPCs and silicon detectors. *Nucl. Instr. and Meth. in Phys. Res. A* **562**, 154 (2006).
26. Zhou, J., Light (anti)Nuclei production in the STAR experiment at RHIC. Ph.D. thesis, Rice University, (2009).

27. Tang, Z. *et al.*, Spectra and radial flow in relativistic heavy ion collisions with Tsallis statistics in a blast-wave description. *Phys. Rev. C* **79**, 051901(R) (2009).
28. Abelev, B. I. *et al.*, STAR Collaboration, Yields and elliptic flow of d (\bar{d}) and ${}^3\text{He}$ (${}^3\bar{\text{He}}$) in Au + Au collisions at $\sqrt{s_{\text{NN}}} = 200$ GeV. e-Print: arXiv:0909.0566 [nucl-ex].
29. Greiner, W., On the extension of the periodic system into the sectors of strangeness and anti-matter. *Int. J. Mod. Phys. E* **5**, 1 (1996).
30. Ahlen, S. *et al.*, An antimatter spectrometer in space. *Nucl. Instr. and Meth. in Phys. Res. A* **350**, 351 (1994).

Acknowledgements We thank the RHIC Operations Group and RACF at BNL, the NERSC Center at LBNL and the Open Science Grid consortium for providing resources and support. This work was supported in part by the Offices of NP and HEP within the U.S. DOE Office of Science, the U.S. NSF, the Sloan Foundation, the DFG cluster of excellence ‘Origin and Structure of the Universe’ of Germany, CNRS/IN2P3, FAPESP CNPq of Brazil, Ministry of Ed. and Sci. of the Russian Federation, NNSFC, CAS, MoST, and MoE of China, GA and MSMT of the Czech Republic, FOM and NWO of the Netherlands, DAE, DST, and CSIR of India, Polish Ministry of Sci. and Higher Ed., Korea Research Foundation, Ministry of Sci., Ed. and Sports of the Rep. Of Croatia, and RosAtom of Russia.

H. Agakishiev¹⁷, M. M. Aggarwal²⁹, Z. Ahammed²¹, A. V. Alakhverdyants¹⁷, I. Alekseev¹⁵, J. Alford¹⁸, B. D. Anderson¹⁸, C. D. Anson²⁷, D. Arkhipkin², G. S. Averichev¹⁷, J. Balewski²², D. R. Beavis², N. K. Behera¹³, R. Bellwied⁴³, M. J. Betancourt²², R. R. Betts⁷, A. Bhasin¹⁶,

A. K. Bhati²⁹, H. Bichsel⁴⁹, J. Bielik⁹, J. Bielikova¹⁰, B. Biritz⁵, L. C. Bland², I. G. Bordyuzhin¹⁵, W. Borowski⁴⁰, J. Bouchet¹⁸, E. Braidot²⁶, A. V. Brandin²⁵, A. Bridgeman¹, S. G. Brovko⁴, E. Bruna⁵², S. Bueltmann²⁸, I. Bunzarov¹⁷, T. P. Burton², X. Z. Cai³⁹, H. Caines⁵², M. Calder⁴, D. Cebra⁴, R. Cendejas⁵, M. C. Cervantes⁴¹, Z. Chajecski²⁷, P. Chaloupka¹⁰, S. Chattopadhyay⁴⁷, H. F. Chen³⁷, J. H. Chen³⁹, J. Y. Chen⁵¹, L. Chen⁵¹, J. Cheng⁴⁴, M. Cherney⁸, A. Chikanian⁵², K. E. Choi³³, W. Christie², P. Chung¹⁰, M. J. M. Codrington⁴¹, R. Corliss²², J. G. Cramer⁴⁹, H. J. Crawford³, S. Dash¹², A. Davila Leyva⁴², L. C. De Silva⁴³, R. R. Debbe², T. G. Dedovich¹⁷, A. A. Derevschikov³¹, R. Derradi de Souza⁶, L. Didenko², P. Djawotho⁴¹, S. M. Dogra¹⁶, X. Dong²¹, J. L. Drachenberg⁴¹, J. E. Draper⁴, J. C. Dunlop², L. G. Efimov¹⁷, M. Elnimr⁵⁰, J. Engelage³, G. Eppley³⁵, M. Estienne⁴⁰, L. Eun³⁰, O. Evdokimov⁷, R. Fatemi¹⁹, J. Fedorisin¹⁷, R. G. Fersch¹⁹, P. Filip¹⁷, E. Finch⁵², V. Fine², Y. Fisyak², C. A. Gagliardi⁴¹, D. R. Gangadharan⁵, A. Geromitsos⁴⁰, F. Geurts³⁵, P. Ghosh⁴⁷, Y. N. Gorbunov⁸, A. Gordon², O. G. Grebenyuk²¹, D. Grosnick⁴⁶, S. M. Guertin⁵, A. Gupta¹⁶, W. Guryan², B. Haag⁴, O. Hajkova⁹, A. Hamed⁴¹, L-X. Han³⁹, J. W. Harris⁵², J. P. Hays-Wehle²², M. Heinz⁵², S. Heppelmann³⁰, A. Hirsch³², E. Hjort²¹, G. W. Hoffmann⁴², D. J. Hofman⁷, B. Huang³⁷, H. Z. Huang⁵, T. J. Humanic²⁷, L. Huo⁴¹, G. Igo⁵, P. Jacobs²¹, W. W. Jacobs¹⁴, C. Jena¹², F. Jin³⁹, J. Joseph¹⁸, E. G. Judd³, S. Kabana⁴⁰, K. Kang⁴⁴, J. Kapitan¹⁰, K. Kauder⁷, H. W. Ke⁵¹, D. Keane¹⁸, A. Kechechyan¹⁷, D. Kettler⁴⁹, D. P. Kikola³², J. Kiryluk²¹, A. Kisiel⁴⁸, V. Kizka¹⁷, S. R. Klein²¹, A. G. Knospe⁵², D. D. Koetke⁴⁶, T. Kollegger¹¹, J. Konzer³², I. Koralt²⁸, L. Koroleva¹⁵, W. Korsch¹⁹, L. Kotchenda²⁵, V. Kouchpil¹⁰, P. Kravtsov²⁵, K. Krueger¹, M. Krus⁹, L. Kumar¹⁸, P. Kurnadi⁵, M. A. C. Lamont², J. M. Landgraf², S. LaPointe⁵⁰, J. Lauret², A. Lebedev², R. Lednicky¹⁷, J. H. Lee², W. Leight²², M. J. LeVine², C. Li³⁷, L. Li⁴², N. Li⁵¹, W. Li³⁹, X. Li³²,

X. Li³⁸, Y. Li⁴⁴, Z. M. Li⁵¹, M. A. Lisa²⁷, F. Liu⁵¹, H. Liu⁴, J. Liu³⁵, T. Ljubicic², W. J. Llope³⁵, R. S. Longacre², W. A. Love², Y. Lu³⁷, E. V. Lukashov²⁵, X. Luo³⁷, G. L. Ma³⁹, Y. G. Ma³⁹, D. P. Mahapatra¹², R. Majka⁵², O. I. Mall⁴, L. K. Mangotra¹⁶, R. Manweiler⁴⁶, S. Margetis¹⁸, C. Markert⁴², H. Masui²¹, H. S. Matis²¹, Yu. A. Matulenko³¹, D. McDonald³⁵, T. S. McShane⁸, A. Meschanin³¹, R. Milner²², N. G. Minaev³¹, S. Mioduszewski⁴¹, A. Mischke²⁶, M. K. Mitrovski¹¹, Y. Mohammed⁴¹, B. Mohanty⁴⁷, M. M. Mondal⁴⁷, B. Morozov¹⁵, D. A. Morozov³¹, M. G. Munhoz³⁶, M. K. Mustafa³², M. Naglis²¹, B. K. Nandi¹³, T. K. Nayak⁴⁷, P. K. Netrakanti³², L. V. Nogach³¹, S. B. Nurushev³¹, G. Odyniec²¹, A. Ogawa², K. Oh³³, A. Ohlson⁵², V. Okorokov²⁵, E. W. Oldag⁴², D. Olson²¹, M. Pachr⁹, B. S. Page¹⁴, S. K. Pal⁴⁷, Y. Pandit¹⁸, Y. Panebratsev¹⁷, T. Pawlak⁴⁸, H. Pei⁷, T. Peitzmann²⁶, C. Perkins³, W. Peryt⁴⁸, S. C. Phatak¹², P. Pile², M. Planinic⁵³, M. A. Ploskon²¹, J. Pluta⁴⁸, D. Plyku²⁸, N. Poljak⁵³, J. Porter²¹, A. M. Poskanzer²¹, B. V. K. S. Potukuchi¹⁶, C. B. Powell²¹, D. Prindle⁴⁹, C. Pruneau⁵⁰, N. K. Pruthi²⁹, P. R. Pujahari¹³, J. Putschke⁵², H. Qiu²⁰, R. Raniwala³⁴, S. Raniwala³⁴, R. L. Ray⁴², R. Redwine²², R. Reed⁴, H. G. Ritter²¹, J. B. Roberts³⁵, O. V. Rogachevskiy¹⁷, J. L. Romero⁴, A. Rose²¹, L. Ruan², J. Rusnak¹⁰, N. R. Sahoo⁴⁷, S. Sakai²¹, I. Sakrejda²¹, S. Salur⁴, J. Sandweiss⁵², E. Sangaline⁴, A. Sarkar¹³, J. Schambach⁴², R. P. Scharenberg³², A. M. Schmah²¹, N. Schmitz²³, T. R. Schuster¹¹, J. Seele²², J. Seger⁸, I. Selyuzhenkov¹⁴, P. Seyboth²³, E. Shahaliev¹⁷, M. Shao³⁷, M. Sharma⁵⁰, S. S. Shi⁵¹, Q. Y. Shou³⁹, E. P. Sichtermann²¹, F. Simon²³, R. N. Singaraju⁴⁷, M. J. Skoby³², N. Smirnov⁵², P. Sorensen², H. M. Spinka¹, B. Srivastava³², T. D. S. Stanislaus⁴⁶, D. Staszak⁵, S. G. Steadman²², J. R. Stevens¹⁴, R. Stock¹¹, M. Strikhanov²⁵, B. Stringfellow³², A. A. P. Suaide³⁶, M. C. Suarez⁷, N. L. Subba¹⁸, M. Sumbera¹⁰, X. M. Sun²¹, Y. Sun³⁷, Z. Sun²⁰, B. Surrow²², D. N. Svirida¹⁵, T. J. M. Symons²¹, A. Szanto de Toledo³⁶,

J. Takahashi⁶, A. H. Tang², Z. Tang³⁷, L. H. Tarini⁵⁰, T. Tarnowsky²⁴, D. Thein⁴², J. H. Thomas²¹,
J. Tian³⁹, A. R. Timmins⁴³, D. Tlusty¹⁰, M. Tokarev¹⁷, T. A. Trainor⁴⁹, V. N. Tram²¹, S. Trentalange⁵,
R. E. Tribble⁴¹, P. Tribedy⁴⁷, O. D. Tsai⁵, T. Ullrich², D. G. Underwood¹, G. Van Buren², G. van Nieuwenhuizen²²,
J. A. Vanfossen, Jr.¹⁸, R. Varma¹³, G. M. S. Vasconcelos⁶, A. N. Vasiliev³¹, F. Videb, Y. P. Viyogi⁴⁷,
S. Vokal¹⁷, S. A. Voloshin⁵⁰, M. Wada⁴², M. Walker²², F. Wang³², G. Wang⁵, H. Wang²⁴, J. S. Wang²⁰,
Q. Wang³², X. L. Wang³⁷, Y. Wang⁴⁴, G. Webb¹⁹, J. C. Webb², G. D. Westfall²⁴, C. Whitten Jr.⁵,
H. Wieman²¹, S. W. Wissink¹⁴, R. Witt⁴⁵, W. Witzke¹⁹, Y. F. Wu⁵¹, Z. Xiao⁴⁴, W. Xie³², H. Xu²⁰,
N. Xu²¹, Q. H. Xu³⁸, W. Xu⁵, Y. Xu³⁷, Z. Xu², L. Xue³⁹, Y. Yang²⁰, Y. Yang⁵¹, P. Yepes³⁵, K. Yip²,
I-K. Yoo³³, M. Zawisza⁴⁸, H. Zbroszczyk⁴⁸, W. Zhan²⁰, J. B. Zhang⁵¹, S. Zhang³⁹, W. M. Zhang¹⁸,
X. P. Zhang⁴⁴, Y. Zhang²¹, Z. P. Zhang³⁷, J. Zhao³⁹, C. Zhong³⁹, W. Zhou³⁸, X. Zhu⁴⁴, Y. H. Zhu³⁹,
R. Zoukarneev¹⁷, Y. Zoukarneeva¹⁷

(STAR Collaboration)

¹Argonne National Laboratory, Argonne, Illinois 60439, USA

²Brookhaven National Laboratory, Upton, New York 11973, USA

³University of California, Berkeley, California 94720, USA

⁴University of California, Davis, California 95616, USA

⁵University of California, Los Angeles, California 90095, USA

⁶Universidade Estadual de Campinas, Sao Paulo, Brazil

⁷University of Illinois at Chicago, Chicago, Illinois 60607, USA

⁸Creighton University, Omaha, Nebraska 68178, USA

- ⁹Czech Technical University in Prague, FNSPE, Prague, 115 19, Czech Republic
- ¹⁰Nuclear Physics Institute AS CR, 250 68 Řež/Prague, Czech Republic
- ¹¹University of Frankfurt, Frankfurt, Germany
- ¹²Institute of Physics, Bhubaneswar 751005, India
- ¹³Indian Institute of Technology, Mumbai, India
- ¹⁴Indiana University, Bloomington, Indiana 47408, USA
- ¹⁵Alikhanov Institute for Theoretical and Experimental Physics, Moscow, Russia
- ¹⁶University of Jammu, Jammu 180001, India
- ¹⁷Joint Institute for Nuclear Research, Dubna, 141 980, Russia
- ¹⁸Kent State University, Kent, Ohio 44242, USA
- ¹⁹University of Kentucky, Lexington, Kentucky, 40506-0055, USA
- ²⁰Institute of Modern Physics, Lanzhou, China
- ²¹Lawrence Berkeley National Laboratory, Berkeley, California 94720, USA
- ²²Massachusetts Institute of Technology, Cambridge, MA 02139-4307, USA
- ²³Max-Planck-Institut für Physik, Munich, Germany
- ²⁴Michigan State University, East Lansing, Michigan 48824, USA
- ²⁵Moscow Engineering Physics Institute, Moscow Russia
- ²⁶NIKHEF and Utrecht University, Amsterdam, The Netherlands
- ²⁷Ohio State University, Columbus, Ohio 43210, USA
- ²⁸Old Dominion University, Norfolk, VA, 23529, USA
- ²⁹Panjab University, Chandigarh 160014, India

³⁰Pennsylvania State University, University Park, Pennsylvania 16802, USA

³¹Institute of High Energy Physics, Protvino, Russia

³²Purdue University, West Lafayette, Indiana 47907, USA

³³Pusan National University, Pusan, Republic of Korea

³⁴University of Rajasthan, Jaipur 302004, India

³⁵Rice University, Houston, Texas 77251, USA

³⁶Universidade de Sao Paulo, Sao Paulo, Brazil

³⁷University of Science & Technology of China, Hefei 230026, China

³⁸Shandong University, Jinan, Shandong 250100, China

³⁹Shanghai Institute of Applied Physics, Shanghai 201800, China

⁴⁰SUBATECH, Nantes, France

⁴¹Texas A&M University, College Station, Texas 77843, USA

⁴²University of Texas, Austin, Texas 78712, USA

⁴³University of Houston, Houston, TX, 77204, USA

⁴⁴Tsinghua University, Beijing 100084, China

⁴⁵United States Naval Academy, Annapolis, MD 21402, USA

⁴⁶Valparaiso University, Valparaiso, Indiana 46383, USA

⁴⁷Variable Energy Cyclotron Centre, Kolkata 700064, India

⁴⁸Warsaw University of Technology, Warsaw, Poland

⁴⁹University of Washington, Seattle, Washington 98195, USA

⁵⁰Wayne State University, Detroit, Michigan 48201, USA

⁵¹Institute of Particle Physics, CCNU (HZNU), Wuhan 430079, China

⁵²Yale University, New Haven, Connecticut 06520, USA

⁵³University of Zagreb, Zagreb, HR-10002, Croatia